

Prepolarized Magnetic Resonance Imaging around Metal Orthopedic Implants

Ross D. Venook,^{1*} Nathaniel I. Matter,¹ Meena Ramachandran,¹ Sharon E. Ungersma,¹ Garry E. Gold,² Nicholas J. Giori,^{3,4} Albert Macovski,¹ Greig C. Scott,¹ and Steven M. Conolly^{1,5}

A prepolarized MRI (PMRI) scanner was used to image near metal implants in agar gel phantoms and in in vivo human wrists. Comparison images were made on 1.5- and 0.5-T conventional whole-body systems. The PMRI experiments were performed in a smaller bore system tailored to extremity imaging with a prepolarization magnetic field of 0.4 T and a readout magnetic field of 27–54 mT (1.1–2.2 MHz). Scan parameters were chosen with equal readout gradient strength over a given field of view and matrix size to allow unbiased evaluation of the benefits of lower readout frequency. Results exhibit substantial reduction in metal susceptibility artifacts under PMRI versus conventional scanners. A new artifact quantification technique is also presented, and phantom results confirm that susceptibility artifacts improve as expected with decreasing readout magnetic field using PMRI. This proof-of-concept study demonstrates that prepolarized techniques have the potential to provide diagnostic cross-sectional images for postoperative evaluation of patients with metal implants. Magn Reson Med 56:177–186, 2006. © 2006 Wiley-Liss, Inc.

Key words: metal artifact; susceptibility artifact; prepolarized MRI; low-field MRI; low-cost MRI

Metal hardware is commonly implanted in orthopedic surgery to reduce and fixate fractures, to replace arthritic joints, and to align and stabilize the spine. In the United States alone, nearly 450000 primary or revision total knee arthroplasties were performed in 2002, representing nearly a threefold increase from 1990 (1). These numbers are growing rapidly with improvements in surgical technology and with the aging population. Because of its unique ability to visualize both osseous structures and adjacent soft tissue, orthopedists frequently rely on MRI for diagnosis and preoperative planning (2). Unfortunately, the physical characteristics of metal implants often make them difficult to image with cross-sectional techniques. Metal

artifacts can severely degrade CT images throughout the field of view, while susceptibility artifacts impair tissue visualization near metal implants under MRI (3,4). Because of these challenges, postoperative progress is difficult to monitor, and complications including loosening can go undiagnosed until another surgery becomes necessary (5). Without proper preoperative images, these revision surgeries are also more difficult to plan and execute.

The basic obstacles to imaging near metal with MR are susceptibility-related static field distortions (6,7), gradient-induced eddy currents on metal surfaces (8), and RF shielding effects (9). Among these, susceptibility is by far the dominant problem in MRI systems. Gradient-echo imaging is almost impossible near metal because local field inhomogeneity causes rapid dephasing and results in signal voids. Spin-echo techniques are more successful because of their rephasing effects, but they still suffer spatially dependent artifacts. For 2D Fourier transform (2DFT) acquisitions, these include correctable shifts/distortions, uncorrectable voids and pile-ups, and T_2^* -related blurring and signal loss.

Specialized pulse sequences have had some success with addressing these artifacts. View angle tilting (VAT) provides an elegant way to correct for general inhomogeneity errors (10). It is particularly effective for correcting chemical shift artifacts and is the basis for most sequences that endeavor to image near metal (4,11). Recent work also provides a method to correct for VAT-associated blurring (12). Unfortunately, VAT is incompatible with 3D imaging and otherwise requires excellent slice selection—which is impossible to ensure in the presence of strong inhomogeneities near metal. Another technique to avoid inhomogeneity artifacts involves encoding and acquiring MR signal from one k -space location at a time. Such “single point” methods can produce almost perfect images near metal, but even the most time-efficient of these sequences are too slow for clinical applications (13).

Correction of susceptibility artifacts through postprocessing is another area of active research. Well-known methods can correct mild inhomogeneities (14,15,16), such as those caused by air–tissue interfaces. Most postprocessing algorithms use some a priori knowledge about the object and/or perform field mapping to “unwrap” the images that result from naive reconstruction. Recent work continues to improve both the outcome and the computational load of these methods (17,18), but none is yet workable in in vivo applications involving metal implants. Moreover, if the field errors are strong enough, as they are near most metals, the encoding becomes ambiguous and simply uncorrectable.

¹Magnetic Resonance Systems Research Laboratory, Department of Electrical Engineering, Stanford University, Stanford, California, USA.

²Department of Radiology, Stanford University, Stanford, California, USA.

³VA Palo Alto Healthcare System, Palo Alto, California, USA.

⁴Department of Orthopedic Surgery, Stanford University, Stanford, California, USA.

⁵Department of Bioengineering, University of California at Berkeley, Berkeley, California, USA.

Grant sponsor: NIH; Grant numbers: NIH R33 EB00777, NIH 1R01 EB0002524, NIH R01 EB00346, NIH 5R24CA092862–03; Grant sponsor: The Whitaker Foundation; Grant sponsor: GE Global Healthcare.

*Correspondence to: Ross D. Venook, 350 Serra Mall, Packard Electrical Engineering Building, Room 063, Stanford University, Stanford, CA 94305-9510, USA. E-mail: ross@mrsrl.stanford.edu

Received 7 November 2005; revised 14 March 2006; accepted 20 March 2006
DOI 10.1002/mrm.20927

Published online 24 May 2006 in Wiley InterScience (www.interscience.wiley.com).

Finally, many studies attempt to minimize distortions, or at least their effect on the diagnostic quality of the images, by manipulating patient (and implant) orientation with respect to the main field (2,19,20). While these all provide relevant data that are clinically applicable, there are significant limitations to the generality and effectiveness of such methods.

All existing methods attempt to avoid or correct for artifacts associated with the necessarily large field disturbances near metal in conventional clinical scanners. Because of the limited success and limited clinical acceptance of these methods, we suggest a different approach. Magnetic field distortion around an object scales with the instantaneous applied field, so imaging at lower fields reduces susceptibility artifacts (21,22). The obvious trade-off with lowering B_0 on a conventional system is loss of signal-to-noise ratio (SNR). We propose to image around metal implants with a prepolarized MRI (PMRI) system that allows for low-field signal acquisition with mid-field SNR.

The PMRI method is a novel form of field-cycled MR imaging that uses two specialized electromagnets instead of one superconducting magnet to create its B_0 field (23,24,25). The first magnet polarizes the sample with a relatively strong (0.4–1.0 T) but not necessarily homogeneous (20% peak-to-peak inhomogeneity) magnetic field pulse. It ramps down as the second magnet ramps up to provide a homogeneous (less than 0.1% peak-to-peak inhomogeneity), stable, low field (20–180 mT, or 1–8 MHz) for reception. Hereafter, B_0 refers to the homogeneous part of the magnetic field that is present during RF excitation and readout operations. Figure 1 displays a system diagram in cross section along with a generic PMRI pulse sequence diagram.

Because of the inexpensive electromagnets (~25000 USD for both prepolarization and readout electromagnets), system costs are much lower for PMRI than for standard MRI. Moreover, the field-cycled nature of the system enables unique flexibilities and contrast mechanisms. What sets a PMRI system apart from conventional low-field scanners is the development of sample polarization at a moderate field strength. This creates initial bulk magnetization that is proportional to the polarization field. As long as the sample noise is larger than the coil noise, the SNR of a prepolarized MR experiment depends only on the polarization field (23,26). Hyperpolarization techniques achieve MR signals in gases that are also far above the Boltzmann equilibrium magnetization at the readout magnetic field strength (27,28,29). However, because PMRI does not involve the dramatically higher diffusion rates of gases, the very short T_2/T_2^* times that are typical in hyperpolarization experiments are not evident with PMRI. One drawback of PMRI is that multislice methods are relatively inefficient because the full volume must experience prepolarization in the same interval. This motivates our use of 3D acquisitions in vivo (30). In this work, prepolarization allows us to reap the benefit of using a low readout field to reduce susceptibility artifacts with only modest reduction in SNR.

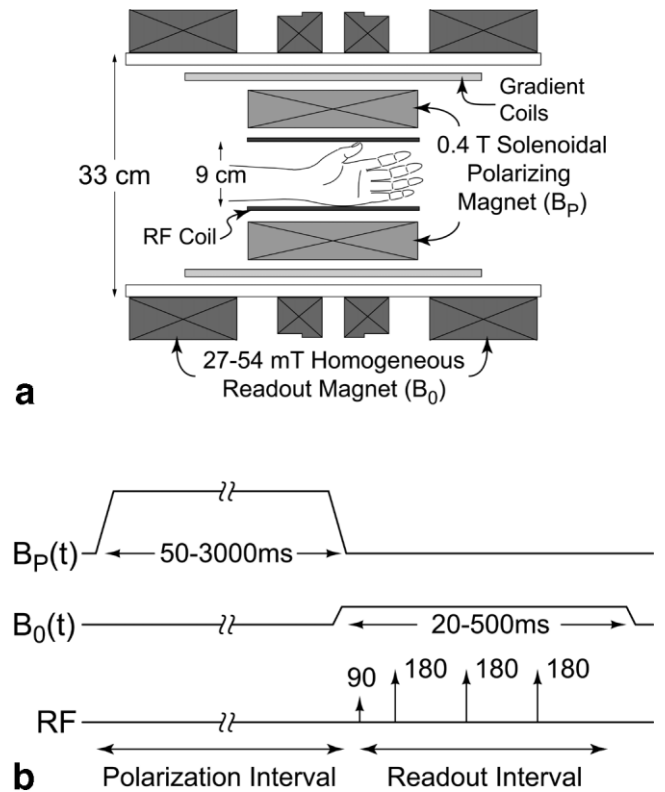


FIG. 1. PMRI system overview. (a) Cross section of the prepolarized wrist imaging system. A 0.4-T solenoidal polarizing magnet (B_P) is coaxial and within the bore of the 27- to 54-mT homogeneous readout magnet (B_0). (b) Sample multiple spin-echo pulse sequence diagram. During the polarization interval, bulk magnetization grows toward the polarizing field equilibrium. After switching B_0 on and B_P off, the magnetization decays toward the B_0 equilibrium. During the readout interval, standard low-field MR acquisition takes place with signal boosted by the prepolarization.

THEORY

This section presents relevant theory along with a new method of quantifying metal susceptibility artifacts. Metal objects, even if they are not ferromagnetic, cause artifacts and distortion in clinical MR images because they have drastically different magnetic susceptibility than human tissue. The susceptibility differences cause local field distortions that vary in space and depend upon the material properties of the objects, their shapes and orientations, and the strength of the applied magnetic field. The resonant frequency shift ($\Delta\omega$) from these field distortions is directly proportional to the susceptibility mismatch ($\Delta\chi$), applied field (B_0), and gyromagnetic ratio (γ), as in $\Delta\omega \propto \Delta\chi\gamma B_0$.

Closed-form expressions for frequency shift as a function of position exist for specific shapes such as a cylinder or a sphere (6). There are also numerical methods of varying complexity and generality for determining the local effects of other shapes, including arbitrary susceptibility distributions (31–33). Whatever their form, spatial inhomogeneities from susceptibility differences have the potential to cause artifacts that we can classify as either dephasing or distorting in nature. Because dephasing is

TABLE 1.
Expected Maximum Magnitude of Shift Artifact of Pixels Directly Adjacent to Cylinders of Common Metal Implant Materials^a

Material	$\Delta\chi^b$ (ppm)	Δx (at 1.5 T)	Δx (at 27 mT)
Air	10	0.38 mm	6.8 μ m
Titanium	191	7 mm	0.12 mm
Chromium	329	12 mm	0.22 mm

^aAssumes 2DFT experiment with 40 mT/m readout gradient and cylinder axis perpendicular to both main magnetic field and readout direction.

^bSusceptibility differences tabulated by Schenck (7).

prohibitive when imaging near metal with gradient-echo techniques at standard field strengths (22), we refer the interested reader to a full discussion elsewhere (34). In this treatment, we will focus on distortion artifacts.

Distortion Artifacts

For standard 2DFT data acquisition methods, off-resonance conditions manifest singularly as a readout-direction displacement of

$$\Delta x = \Delta\omega/\gamma G_r \propto \Delta\chi B_0/G_r, \quad [1]$$

where G_r is the strength of the readout gradient. Equation [1] explains why susceptibility-induced distortion artifacts generally become worse with higher magnetic field strengths during the readout period (21), while increasing readout gradient strength improves these artifacts (4). Because the PMRI scanner in this study acquires data at a low static field (27–54 mT, or 1.1–2.2 MHz) without necessarily losing gradient strength, we expect improvements in the readout-direction shifts due to metal implants by a factor between 1.5 T/27 mT = 57 and 1.5 T/54 mT = 28 versus a 1.5-T system. Table 1 contains calculated maximum shifts for cylinders of different common implant materials at different readout magnetic field strengths. A 7-mm displacement due to titanium at 1.5 T may obscure important anatomy, while the artifact would be a benign 0.12-mm shift at 27 mT.

Uncorrectable Distortion

Although Table 1 presents the expected worst-case shifts for tissue directly adjacent to metal, there is no indication of the object size: the maximum shift is only dependent on the materials involved and is always highest at their interface. The shift falls off with distance from the interface, so signal from voxels near the metal will get displaced further along the readout direction than signal from more distant voxels. In certain cases, this spatial distribution leaves voids near the susceptibility/material boundary and piles signal at the edges of the void. This creates unrecoverable errors in the reconstruction because signal from many different voxels becomes encoded into the same pixel. Physically, such pile-up occurs whenever the local inhomogeneity gradient is equal and opposite the readout gradient. Ludeke et al. (6) have derived a simple criterion for this condition. Relating B_0 , $\Delta\chi$, G_r , R (object radius), and α

(a geometrical constant between 0 and 1), the condition for creating uncorrectable distortion is

$$|\gamma_c| = \alpha\Delta\chi B_0/RG_r = \alpha\Delta x/R > 1/2, \quad [2]$$

which corresponds to a field error that exceeds the gradient field range over the width of the object. This means that smaller objects will more readily experience pile-up artifacts, since the susceptibility-induced gradient is steeper near a smaller object. Given a B_0 , $\Delta\chi$, and maximum G_r , Eq. [2] allows us to calculate the minimum object radius for avoiding uncorrectable distortion. Figure 2 displays a plot of γ_c versus object diameter for a titanium cylinder using 3 mT/m (0.3 G/cm) gradients at 1.5 T and 27 mT, corresponding to the conditions of the screw phantom experiments in this work. We needed to use low gradient strengths to generate uncorrectable artifacts in the PMRI images, but even with 40 mT/m (4 G/cm) gradients (Fig. 3) we calculate that a titanium cylinder must be greater than 1.2 cm wide to allow proper reconstruction of nearby tissue at 1.5 T. This minimum feature size is about 0.5 mm wide under PMRI at either 27 or 54 mT with the higher gradient strength. Hence, one would hypothesize the absence of pile-up artifacts in a prepolarized MRI scan of all but the smallest (or most magnetic) metal objects.

Measuring Susceptibility Artifacts in Images

To demonstrate the artifact improvement in our PMRI scanner, compared to a conventional 1.5-T scanner, we have developed a technique for measuring pile-up artifacts in images and comparing the measurements with theory. Quantification studies exist for metal artifacts (11,22,35), but to our knowledge, none have yet linked their measurements with theory.

Quantifying susceptibility artifacts in uncorrectably distorted images can be difficult because of the ambiguity in

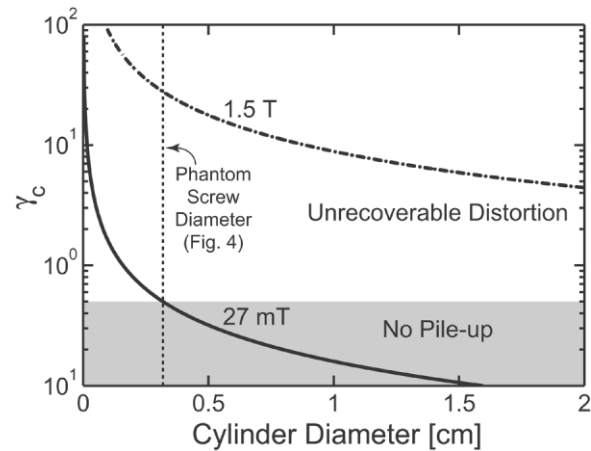


FIG. 2. Graph of condition for uncorrectable image distortion ($\gamma_c > 1/2$) versus diameter for a cylinder of titanium alloy at 1.5 T and 27 mT main field strengths with 3 mT/m gradient ($\Delta\chi = 182$ ppm). This small gradient was the strongest we could use and still produce uncorrectable distortion around the 4-mm titanium screws in the phantom experiment in Fig. 5 (as indicated by the vertical dotted line).

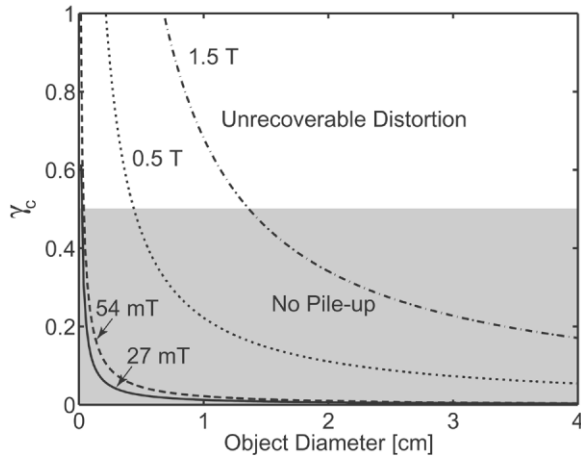


FIG. 3. Graph of condition for uncorrectable image distortion ($\gamma_c > 1/2$) versus diameter for a cylinder of titanium alloy at various field strengths with 40 mT/m gradient ($\Delta\chi = 182$ ppm). Using Eq. [2], we expect pile-up artifacts for tissue near cylinders with diameter < 1.2 cm at 1.5 T. PMRI images should be correctable for pins as small 0.5 mm in diameter at either 27 or 54 mT with 40 mT/m gradient strength.

the location of the signal sources that reconstruct to certain image pixels. One unambiguous feature, however, is the border between the signal void and signal pile-up at the tip of the arrowhead artifact that is typically adjacent to the metal object and pointing in the readout direction (see figures herein). With a known object position, displacement between the object and artifact boundaries is measurable in an image. Because there is also an analytical relationship governing this displacement, we can quantify artifact improvement in a rigorous way. For a cylinder with axis perpendicular to both the main magnetic field and the readout direction, we quantify the artifact as the distance z' from the cylinder center to the pile-up edge in the readout direction, which has the theoretical form

$$z' = \frac{3}{2} \sqrt[3]{\Delta\chi B_0 R^2 / G_r}. \quad [3]$$

Details of this analysis are in the Appendix.

METHODS

We compared the ability of our PMRI scanner to image near metal orthopedic implants with that of a conventional 1.5-T GE Signa scanner and an interventional GE Signa SP 0.5-T scanner (General Electric, Milwaukee, WI, USA). The PMRI system in these experiments is a small-bore scanner for extremity imaging with a clear bore diameter of 9 cm. All PMRI experiments used a 0.4-T prepolarization field with either a 27 or a 54 mT readout static magnetic field. We first performed imaging experiments with metal implants and a plastic grid within agarose gel phantoms. We then imaged metallic hardware within in vivo human wrists.

Orthopedic Screw and Tibial Implant Phantoms

To analyze metallic implant effects in phantoms with homogeneous background signal, we constructed and imaged an orthopedic screw phantom and a tibial implant phantom. Figure 4 displays the experimental setup for the titanium alloy tibial implant (Howmedica, Rutherford, NJ, USA). The setup for the screw phantom is somewhat smaller and contains two 34-mm-long, 4-mm-diameter coated titanium screws (Alphatec, Carlsbad, CA, USA). In both cases, we mounted the metal onto a plastic grid ($15 \times 15 \times 9$ mm units) and suspended this in a cylindrical plastic container filled with agarose gel. We doped the gel with copper sulfate at 2.3 g/liter (14.7 mM, $T_1 = T_2 = 100$ ms at 1.5 T). For imaging, we oriented the phantom coaxially with the bore at isocenter in all scanners.

Imaging parameters for the phantom experiments are given in Table 2. We chose to use equal readout gradients for all three systems to allow comparisons based upon main field strength. We did this by holding the bandwidth/field of view ratio constant across the systems. To ensure comparison of appropriate slices we used the aspect ratio

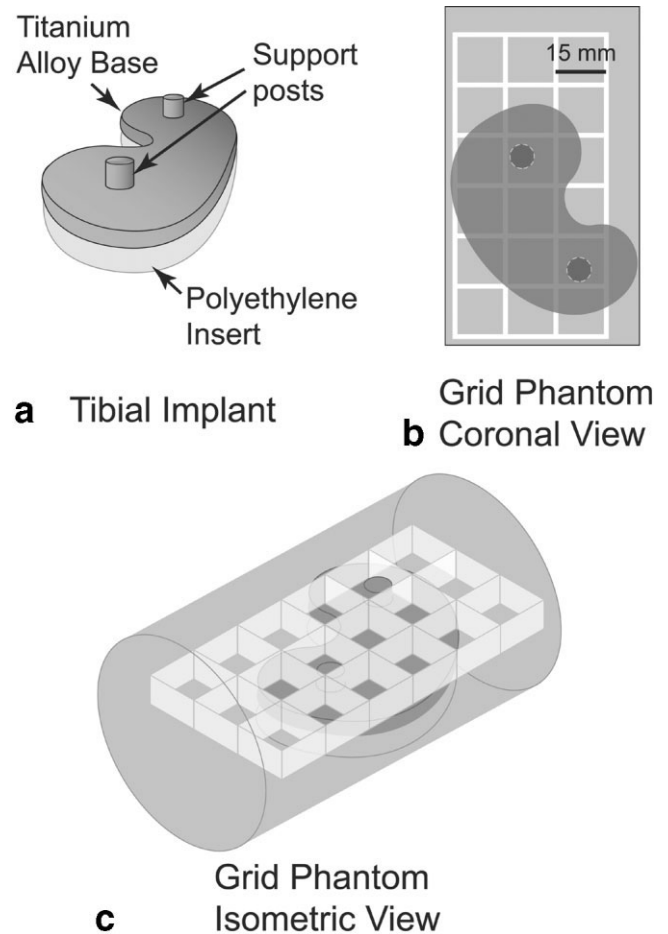


FIG. 4. Phantom diagram of titanium alloy tibial base plate and plastic grid in a plastic cylinder of agarose gel. (a) Perspective view of tibial implant (shown inferior-side up, for clarity). (b) Coronal projection of implant in grid phantom. (c) Isometric view of phantom. Note that posts partially fill two grid squares. Grid squares measure $15 \times 15 \times 9$ mm.

TABLE 2.
Sequence Parameters for Conventional MRI (1.5 T) and PMRI (27 or 54 mT) Experiments^{a,b}

Object	Image plane	Seq. ^{c,d}	B ₀ field	Image matrix	Slice (mm)	FOV (cm ²)	±BW (kHz)	G _r (mT/m)	TE/TR (ms/ms)	Scan time ^e
Screw Phantom	COR	SE	1.5 T	128 × 128	5	12	8	3	15/300	2:01
	COR	SE	27 mT	128 × 128	5	12	8	3	8/150	1:20
Tibial Phantom	COR	SE	1.5 T	128 × 128	5	12	15.6	6	17/1000	2:20
	COR	SE	0.5 T	128 × 128	5	12	15.6	6	16/1000	2:20
	COR	SE	27 mT	128 × 128	5	12	15.6	6	9/500	1:20
In vivo Wrists	COR	RARE	1.5 T	192 × 192	3	10	25	9	17/1000	6:26
	COR	RARE	54 mT	192 × 192	3	10	24	9	9/500	4:35
	AX	RARE	1.5 T	192 × 192	5	10	25	9	17/1000	6:12
	AX	RARE	54 mT	192 × 192	5	10	24	9	9/500	4:35

^aReadout direction S/I-parallel to the main field direction for all coronal images and R/L for all axial images.

^bPrepolarization of 0.4 T for the PMRI scans.

^cMultislice spin echo (SE) sequences with conventional systems; single-slice spin echo sequences with PMRI.

^d*In vivo* images acquired with 3D RARE acquisitions using 16 phase encodes in the slice direction.

^eScan times included for completeness, but do not represent scanner limitations.

of the agar gel along with the plastic grid as fiducials. We empirically adjusted the slice position in the PMRI experiments to match the 1.5-T slices. We increased the echo and repetition times with increasing readout field to account for differences in relaxation times, matching contrast while sacrificing some SNR for longer echo times. As spin echo techniques are refocused, distortion artifacts are unaffected by changes in echo time.

Artifact Quantification

We used the screw phantom images to quantify artifact scaling with readout field strength, comparing the results with analytical solutions for long cylinders perpendicular to both the readout direction and the main magnetic field. We used reduced gradients and a small-diameter screw in order to create pile-up artifacts for measurement at low field. To process the images, we used the regular plastic grid shape as a reference to determine the actual location of each screw. We then counted the pixels along the readout direction from the screw center to the first bright pixel on the void/pile-up boundary using custom software written in MATLAB (The Mathworks, Natick, MA, USA). Performing this procedure for both screws, across multiple image planes from each scanner, we found measurement variation of ± 1 pixel. A figure depicting this procedure is in the Appendix.

Human Wrist Imaging

We used our PMRI scanner and a conventional 1.5-T scanner to image both wrists of a 20-year-old female volunteer. One wrist had a scaphoid fracture fixated with a titanium screw. The other wrist had a steel plate along the distal radius, with four screws in the radial epiphysis and three screws in the radial metaphysis. Both procedures occurred 20 weeks prior to imaging.

In order to image the subjects at isocenter at 1.5 T, we used a transmit/receive quadrature extremity coil with each wrist above the volunteer's head. With the PMRI system, each volunteer sat next to the scanner, resting his/her arm within the bore.

We imaged each wrist with RARE sequences using high system bandwidth (± 25 kHz) over a 10-cm FOV on both systems (36,37). We used a 3D RARE sequence because slice selection is unreliable near metal and because PMRI's SNR efficiency with 3D methods approaches that of conventional MRI (30), reducing volunteer imaging time. We performed all imaging under IRB approval. *In vivo* imaging parameters are given in Table 2. We chose comparable slices based on anatomy, and we increased the readout magnetic field to 54 mT because of increases in SNR associated with improvements in RF coil performance (26). We used longer echo and repetition times at 1.5 T rather than at 54 mT to achieve similar contrast.

RESULTS

Here we present results of artifact quantification in an orthopedic screw phantom, proceeding to images of a tibial plate phantom, and finally to images of orthopedic hardware in two *in vivo* volunteer wrists.

The images in Fig. 5 demonstrate the drastic difference between susceptibility artifacts at 1.5 T and those at lower readout frequency with PMRI (27 mT). The distance from the center of each screw to the boundary between the void and the pile-up in the readout direction measured 21 pixels (± 1) in the 1.5-T images and 6 pixels (± 1) in the PMRI images. Theory predicts this measure to scale with the cube-root of readout magnetic field strength (see Appendix), or $\sqrt[3]{1.5T/27mT} = 3.8$. We measured 21 pixels/6 pixels = 3.5, which is within the uncertainty of the measurement. Changing echo and repetition times (TE and TR) while maintaining gradient strength (BW/FOV) did not measurably affect image artifacts.

Figure 6 displays equal gradient strength images of an agarose gel grid phantom on the three systems, with and without a titanium tibial base plate. The images without the implant provide a basis for evaluating intrinsic distortion in each scanner system; although noticeable at the ends of the bottle, the regular grid demonstrates that such effects are negligible near the isocenter. The PMRI image has almost no susceptibility-induced distortion or drop-

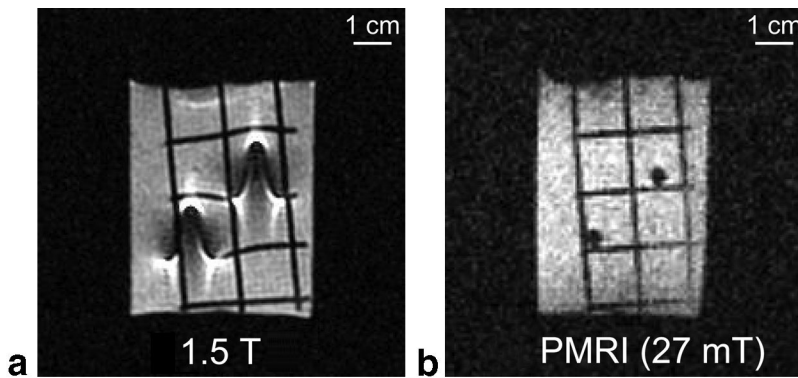


FIG. 5. Coronal images of agarose grid phantom with titanium alloy screws at 1.5 T and 27 mT (PMRI) with 0.4-T prepolarization. (a) Characteristic “arrowhead” artifacts and distortion are substantial at 1.5 T. The pile-up artifact is displaced 21 pixels from the nominal center of the screw. (b) The PMRI image has no visible distortion, with only minor arrowhead artifacts at 6 pixels from the screw center. The main field and readout directions are both toward the top of the page. Table 2 gives imaging parameters for each system.

out, with the holes on the grid corresponding to the metal posts in the object. The 1.5- and 0.5-T images, in contrast, have severe pile-up artifacts, large voids, and substantial distortion. The dependence of susceptibility artifacts on field strength is evident.

Comparison images of an in vivo human wrist with a scaphoid screw are shown in Fig. 7. The 1.5-T image displays the characteristic “arrowhead” artifact, while the PMRI image has no evidence of distortion or artifact. Figure 8 displays radiographs and coronal and axial compar-

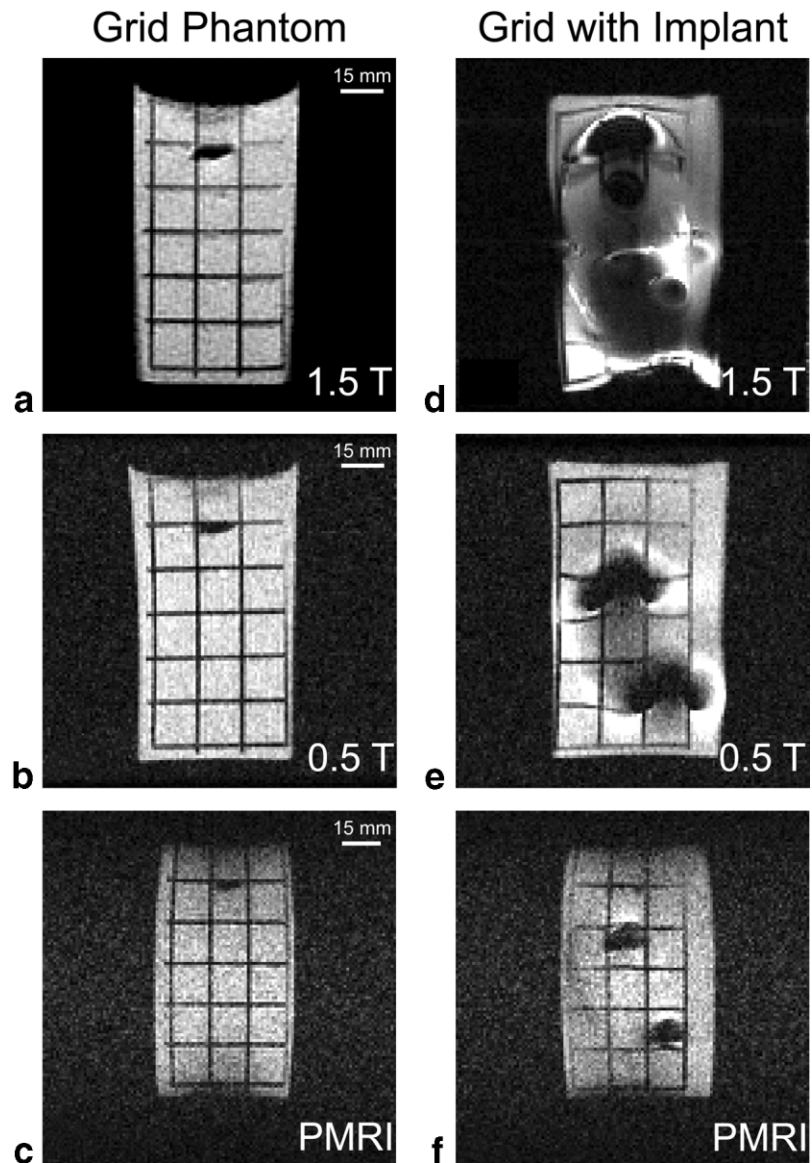
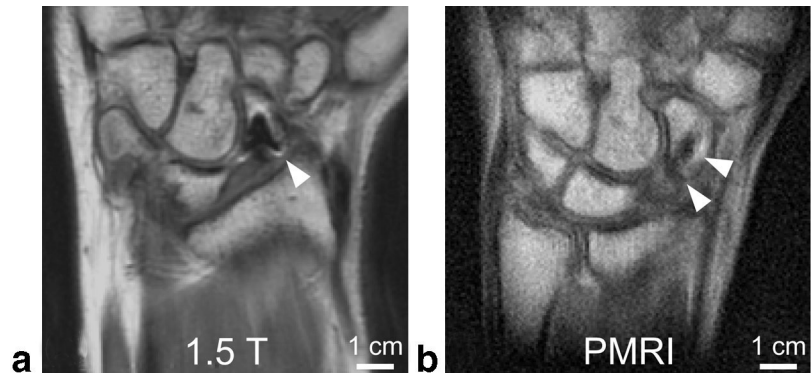


FIG. 6. Coronal images of an agarose grid phantom, without (a,b,c) and with (d,e,f) titanium alloy tibial implant, imaged at 1.5 T, 0.5 T, and 27 mT (PMRI, with 0.4-T prepolarization). Susceptibility-induced distortion from the implant is substantial at 1.5 T (d), but is less so at 0.5 T (e). PMRI image (f) accurately depicts holes in the agar gel from the implant posts with significantly reduced artifacts. The main field and readout direction both point toward the top of the page, and Table 2 gives imaging parameters for each system.

FIG. 7. In vivo comparison images. (a) In a coronal 3D RARE wrist image of a volunteer with a titanium alloy scaphoid screw (arrows), the screw causes a severe artifact at 1.5 T, obscuring much of the scaphoid. (b) With PMRI (54 mT with 0.4-T prepolarization), the bone around the screw is clearly depicted, along with the proximal pole of the scaphoid and the site of the former fracture. Main field and readout direction are toward the top of the page. Image parameters are given in Table 2.



ison images of an in vivo human wrist with metal fixation of a fracture in the volunteer's distal radius. Because of the severity of the artifact from the steel plate, the 1.5-T images (left) are essentially nondiagnostic. The PMRI images clearly show relevant anatomy throughout the forearm and wrist. Due to their sharp feature size, the screw threads

may be causing local signal pile-up artifacts about the screws in both the PMRI and 1.5-T images.

DISCUSSION

This work demonstrates the reduction of susceptibility artifacts that accompanies an MRI experiment with lower

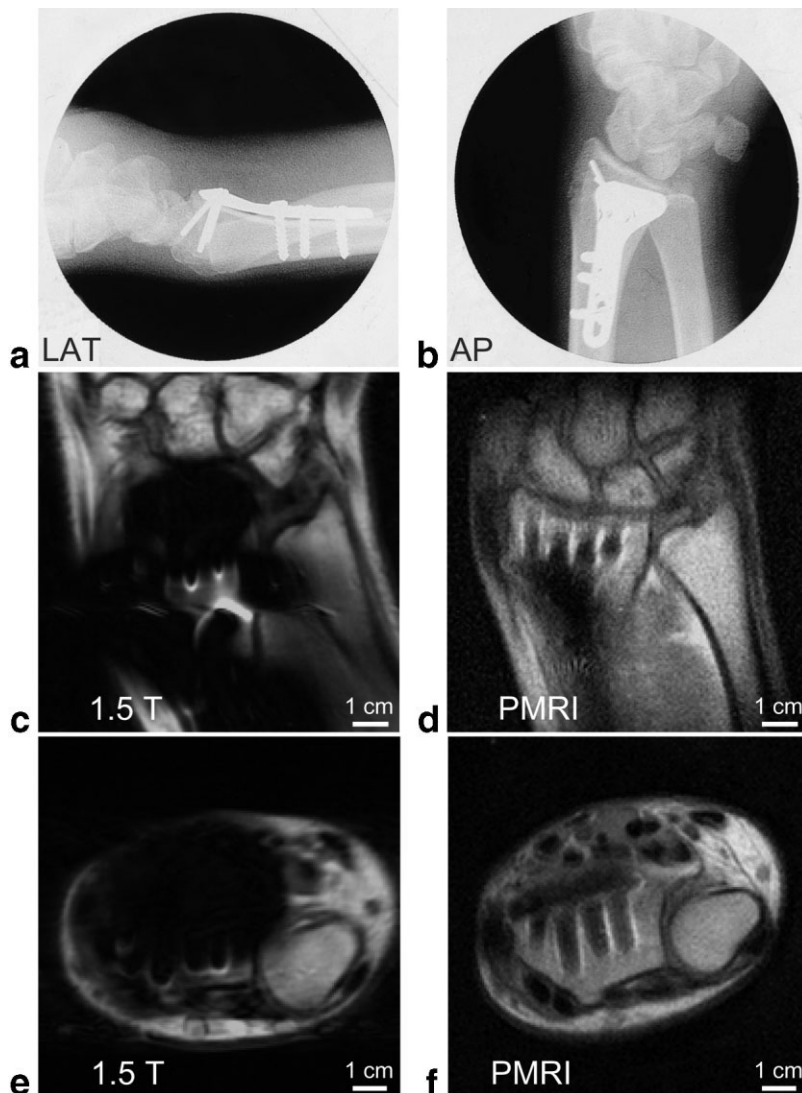


FIG. 8. Lateral and AP radiographs (a,b) with coronal (c,d) and axial (e,f) 3D RARE MR images of an in vivo human wrist with a metal plate and screws. (c,e) Pile-up, signal loss, and distortion artifacts render useless the 1.5-T images. (d,f) The plate and screws in the PMRI images (54 mT, with 0.4-T prepolarization) have only minor artifacts, however, making it possible to visualize the alignment of the radiocarpal joint, the distal radioulnar joint, and the flexor and extensor tendons near the plate. Table 2 gives imaging parameters for the MRI experiments.

readout magnetic field. As expected, PMRI images containing metal orthopedic hardware have significantly smaller susceptibility artifacts compared with either conventional 1.5- or 0.5-T images. The presented method for quantifying these artifacts, relating void extent to the cube-root of imaging field, is in agreement with experimental results in phantoms. Finally, *in vivo* images qualitatively confirm that combining low-field reception with prepolarization allows imaging near metal objects with adequate SNR in reasonable scan times.

There are many well-developed techniques for reducing metal susceptibility artifacts in MRI (4,38). Our experiments did not employ any special methods for artifact reduction. Instead, we chose to compare simple spin-echo and 3D RARE sequences, with equal readout gradient strengths on each of three systems, to provide direct comparisons with respect to readout field. Additionally, to assess realistic clinical postoperative imaging, we compared 3D RARE sequences using different TE and TR on the different systems to yield similar soft tissue contrast in the nonartifactual regions *in vivo*. We could adapt artifact reduction techniques (such as VAT and MARS) to PMRI and expect to achieve similar gains as with conventional scanners. However, the multislice nature of these methods make them less SNR-efficient under PMRI because magnetization only polarizes to the 0.4-T equilibrium during the polarization interval (see Fig. 1), which is foreshortened in the case of multislice imaging in which each slice excitation must follow its own polarization interval. This makes multislice methods no more SNR-efficient than multiple single-slice experiments with PMRI and, together with the robustness of 3D sequences with respect to slice selection artifacts near metal, motivated our use of 3D RARE for *in vivo* imaging (30).

As mentioned under Methods, this work does not present any gradient-echo images because they exhibit substantial dephasing voids in the presence of metal at nearly any readout frequency. However, even with spin-echo techniques, static inhomogeneities can cause dephasing artifacts because the signal is completely rephased only at the exact center of the echo. If the inhomogeneity gradient is strong with respect to the readout gradient, the beginning and end of the acquisition interval will lose signal. This manifests as spatially dependent blurring artifacts and signal loss. To avoid significant signal loss, T_2^* should be at least as long as the data acquisition interval—ensuring less than 2π of dephasing across a voxel at any time during acquisition. Since frequency-encoding relies on creating exactly 2π radians across each voxel during the same interval, this condition exists when the susceptibility-induced inhomogeneity in a voxel equals the readout gradient “inhomogeneity.” This rough requirement does not take into account the fact that most sequences acquire nonisotropic voxels, however, so dephasing artifacts will vary substantially with readout direction and object shape. In these experiments, using longer TE and TR for the conventional scanner images could have lead to greater dephasing artifacts, but separate preliminary experiments verified the dominance of susceptibility artifacts in our experimental protocol.

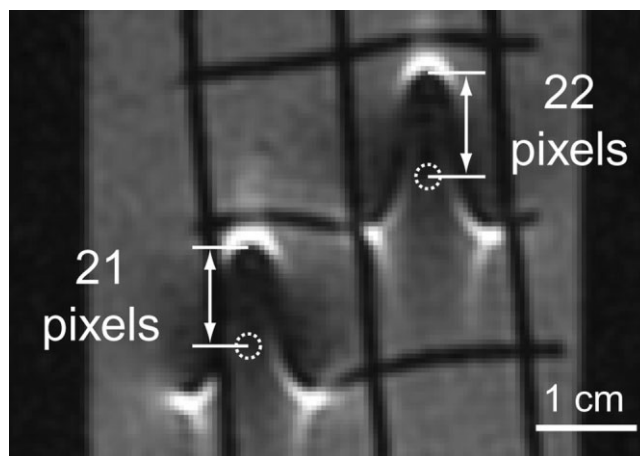


FIG. 9. Artifact measurement example, coronal image of an agarose gel phantom with grid and titanium alloy screws at 1.5 T (from Fig. 5). Although distorted in areas, the grid enables repeatable and accurate location of the center of each screw.

Although this work presents certain benefits of low-field reception, one cannot efficiently receive the SNR boost from prepolarization at arbitrarily low readout fields using simple receiver coils. The reception frequency should be high enough that the dominant noise power in the receive chain comes from the sample. According to Chronik et al., this “body noise dominance” occurs above 5 MHz (125 mT) for a human head, with smaller samples requiring higher frequencies (26). This sets up a direct compromise between SNR and artifact reduction in PMRI, especially for imaging smaller extremities, and we plan to exploit the flexibility of our system to empirically determine optimum operating parameters in future studies.

This work addresses only the susceptibility artifacts in imaging metal under MR. Metal objects can also disturb MR experiments through the local eddy currents of RF excitation or gradient switching, and these effects may not scale down with lower readout frequency (depending on object size). The gradient-switching artifacts are of less concern at present because they vanish near the isocenter. In contrast, RF eddy currents in the metal implants could dominate susceptibility artifacts below some readout frequency because the skin depth remains small in most conductors until well below 1 MHz. However, the RF heating that limits pulse design on conventional scanners scales with the square of Larmor frequency. As such, PMRI can safely employ adiabatic pulses to ensure true RF tip angles—even in the vicinity of metal.

The proof-of-concept nature of the current study opens several new avenues for investigation. Future work should systematically evaluate which combination of imaging techniques and field strengths will produce the best images near metal in a PMRI scanner. Once optimized, PMRI must be rigorously compared to conventional scanners in a best-versus-best study with images graded by radiologists for level of artifact and clinical quality. Because of the limitations of conventional MR scanners and other techniques for imaging near metal, findings during revision surgery will be the gold

standard for validating the sensitivity and specificity of PMRI near metal. The substantial reduction of metal susceptibility artifacts has the potential to make PMRI images much more sensitive and specific than the best conventional MRI images in such a study.

CONCLUSIONS

We have presented comparison images between our PMRI scanner and clinical 1.5- and 0.5-T scanners that highlight the advantage of low-field signal reception for reducing susceptibility artifacts from metal orthopedic hardware. The quality of the PMRI images demonstrates the unique capability of this system to image near metal implants using MRI. The development of a prepolarized MRI system could present an important step forward in the postoperative monitoring and management of patients with orthopedic implants.

APPENDIX

Quantifying Susceptibility Artifacts

This section derives an equation for relating a measurable susceptibility artifact feature to relevant imaging parameters in an uncorrectably distorted imaging experiment. In this study, we use an object with known susceptibility and a closed-form field distortion function: a tall metal cylinder with axis perpendicular to the applied magnetic field. However, the method we describe is general and applies to both analytical and numerical field distortion expressions. Figure 9 displays an example that demonstrates quantification of image artifacts.

Given a gradient, or encoding field, and a susceptibility-induced main field distortion, we can choose a convenient trajectory along the image for analysis. For this experiment—coronal 2DFT imaging of a phantom with a vertically oriented cylinder and readout along the main field direction—we chose the in-plane line through the center of the cylinder that is in the readout/main field direction.

The field offset from B_0 at each location in space is the sum of the susceptibility-induced distortion (ΔB_{SUSC}) and the field offset due to the readout gradient (ΔB_{G}). The susceptibility-induced distortion about a cylinder is (6)

$$\Delta B_{\text{SUSC}}(x,z) = \frac{\Delta\chi B_0 R^2}{2z^2} \left(\frac{z^2 - x^2}{(z^2 + x^2)^2} \right). \quad [4]$$

$$\Delta B_{\text{SUSC}}(0,z) = \frac{\Delta\chi B_0 R^2}{2z^2}. \quad [5]$$

The field from the readout gradient (with possible offset δ) is simply

$$\Delta B_{\text{G}}(x,z) = Gz + \delta. \quad [6]$$

The sum of Eq. [5] and Eq. [6] is the field offset at a given voxel along $x = 0$:

$$\Delta B_{\text{T}}(x,z) = \Delta B_{\text{SUSC}}(x,z) + \Delta B_{\text{G}}(x,z) \quad [7]$$

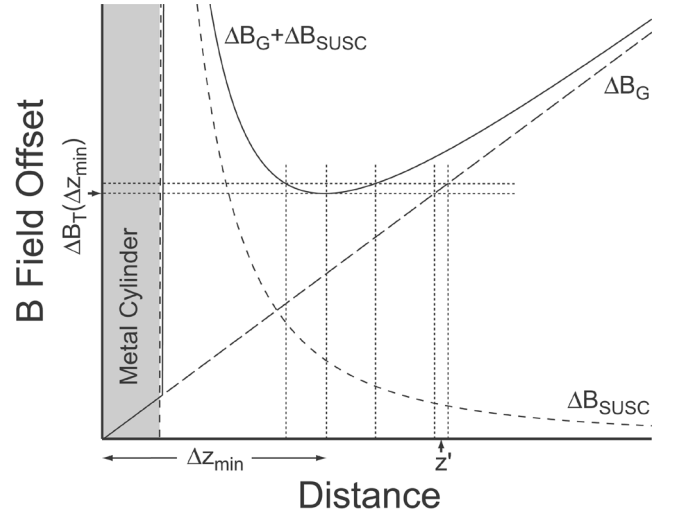


FIG. 10. Graph of magnetic field offsets due to susceptibility distortion (ΔB_{SUSC}), readout gradient (ΔB_{G}), and their sum (from Eq. [7]). The edge between void and pileup is the z' pixel. The signal from all voxels within a distance $\sim \Delta z_{\text{min}}$ from the cylinder center are misregistered to a position that is a distance z' or greater away from the cylinder center.

$$\Delta B_{\text{T}}(0,z) = \frac{\Delta\chi B_0 R^2}{2z^2} + Gz + \delta. \quad [8]$$

Referring to Fig. 10, we can see graphically that any minimum in the field offset (ΔB_{T}) will create ambiguity during reconstruction. To find this minimum, and its position in the readout direction, we set the derivative equal to zero and solve for Δz_{min} :

$$\frac{d\Delta B_{\text{T}}}{dz} = -\frac{\Delta\chi B_0 R^2}{z^3} + G = 0. \quad [9]$$

Solving this equation for z , we find the position (Δz_{min}) at which the local field gradient is zero:

$$\Delta z_{\text{min}} = \sqrt[3]{\frac{\Delta\chi B_0 R^2}{G}}. \quad [10]$$

Assuming naive reconstruction, the signal in the few voxels about Δz_{min} will all be encoded to the same pixel of the image along the readout direction. Also, all of the signal between the object and Δz_{min} will be encoded at points further along the readout direction, ensuring that the signal from Δz_{min} in object space is piled up at the edge of an image void.

To solve for the location of this edge (z'), we plug Δz_{min} into the encoding function (which is just $\Delta B_{\text{G}}(z)$ because we assume simple reconstruction in this case):

$$z' = \frac{\Delta B_{\text{T}}(\Delta z_{\text{min}}) - \delta}{G} \quad [11]$$

$$= \frac{\Delta\chi B_0 R^2}{2G\Delta z_{\min}^2} + \Delta z_{\min} \quad [12]$$

$$= \frac{3}{2} \sqrt[3]{\frac{\Delta\chi B_0 R^2}{2G}}. \quad [13]$$

REFERENCES

- Kurtz S, Mowat F, Ong K, Chan N, Lau E, Halpern M. Prevalence of primary and revision total hip and knee arthroplasty in the United States from 1990 through 2002. *J Bone Joint Surg Am* 2005;87:1487–1497.
- Eustace S, Goldberg R, Williamson D, Melhem ER, Oladipo O, Yucel EK, Jara H. MR imaging of soft tissues adjacent to orthopaedic hardware: techniques to minimize susceptibility artefact. *Clin Radiol* 1997;52:589–594.
- Augustiny N, von Schulthess GK, Meier D, Bosiger P. MR imaging of large nonferromagnetic metallic implants at 1.5 T. *J Comput Assist Tomogr* 1987;11:678–683.
- Olsen RV, Munk PL, Lee MJ, Janzen DL, MacKay AL, Xiang QS, Masri B. Metal artifact reduction sequence: early clinical applications. *Radiographics* 2000;20:699–712.
- White LM, Kim JK, Mehta M, Merchant N, Schweitzer ME, Morrison WB, Hutchison CR, Gross AE. Complications of total hip arthroplasty: MR imaging-initial experience. *Radiology* 2000;215:254–262.
- Ludeke KM, Roschmann P, Tischler R. Susceptibility artefacts in NMR imaging. *Magn Reson Imaging* 1985;3:329–343.
- Schenck JF. The role of magnetic susceptibility in magnetic resonance imaging: MRI magnetic compatibility of the first and second kinds. *Med Phys* 1996;23:815–850.
- Graf H, Steidle G, Martirosian P, Lauer UA, Schick F. Metal artifacts caused by gradient switching. *Magn Reson Med* 2005;54:231–234.
- Camacho CR, Plewes DB, Henkelman RM. Nonsusceptibility artifacts due to metallic objects in MR imaging. *J Magn Reson Imaging* 1995;5:75–88.
- Cho ZH, Kim DJ, Kim YK. Total inhomogeneity correction including chemical shifts and susceptibility by view angle tilting. *Med Phys* 1988;15:7–11.
- Kolind SH, MacKay AL, Munk PL, Xiang QS. Quantitative evaluation of metal artifact reduction techniques. *J Magn Reson Imaging* 2004;20:487–495.
- Butts K, Pauly JM, Gold GE. Reduction of blurring in view angle tilting MRI. *Magn Reson Med* 2005;53:418–424.
- Ramos-Cabrer P, van Duynhoven JPM, Van der Toorn A, Nicolay K. MRI of hip prostheses using single-point methods: in vitro studies towards the artifact-free imaging of individuals with metal implants. *Magn Reson Imaging* 2004;22:1097–1103.
- Sekihara K, Kuroda M, Kohno H. Image restoration from non-uniform magnetic field influence for direct Fourier NMR imaging. *Phys Med Biol* 1984;29:15–24.
- O'Donnell M, Edelstein WA. NMR imaging in the presence of magnetic field inhomogeneities and gradient field nonlinearities. *Med Phys* 1985;12:20–26.
- Jezzard P, Balaban RS. Correction for geometric distortion in echo planar images from B0 field variations. *Magn Reson Med* 1995;34:65–73.
- Skare S, Andersson JLR. Correction of MR image distortions induced by metallic objects using a 3D cubic B-spline basis set: application to stereotactic surgical planning. *Magn Reson Med* 2005;54:169–181.
- Pauchard Y, Smith MR, Mintchev MP. Improving geometric accuracy in the presence of susceptibility difference artifacts produced by metallic implants in magnetic resonance imaging. *IEEE Trans Med Imaging* 2005;24:1387–1399.
- Viano AM, Gronemeyer SA, Haliloglu M, Hoffer FA. Improved MR imaging for patients with metallic implants. *Magn Reson Imaging* 2000;18:287–295.
- Guermazi A, Miaux Y, Zaim S, Peterfy CG, White D, Genant HK. Metallic artefacts in MR imaging: effects of main field orientation and strength. *Clin Radiol* 2003;58:322–328.
- Farahani K, Sinha U, Sinha S, Chiu LC, Lufkin RB. Effect of field strength on susceptibility artifacts in magnetic resonance imaging. *Comput Med Imaging Graph* 1990;14:409–413.
- Olsrud J, Latt J, Brockstedt S, Romner B, Bjorkman-Burtscher IM. Magnetic resonance imaging artifacts caused by aneurysm clips and shunt valves: dependence on field strength (1.5 and 3 T) and imaging parameters. *J Magn Reson Imaging* 2005;22:433–437.
- Macovski A, Conolly S. Novel approaches to low-cost MRI. *Magn Reson Med* 1993;30:221–230.
- Morgan P, Conolly S, Scott G, Macovski A. A readout magnet for prepolarized MRI. *Magn Reson Med* 1996;36:527–536.
- Matter NI, Scott GC, Grafendorfer T, Macovski A, Conolly SM. Rapid polarizing field cycling in magnetic resonance imaging. *IEEE Trans Med Imaging* 2006;25:84–93.
- Chronik BA, Venook RV, Conolly SM, Scott GC. Readout frequency requirements for dedicated prepolarized and hyperpolarized-gas MRI systems. In: *Proceedings of the 10th Annual Meeting of ISMRM, Honolulu, HI, USA, 2002*. p. 58.
- Albert MS, Cates GD, Driehuys B, Happer W, Saam B, Springer CSJ, Wishnia A. Biological magnetic resonance imaging using laser-polarized ^{129}Xe . *Nature* 1994;370:199–201.
- Middleton H, Black RD, Saam B, Cates GD, Cofer GP, Guenther R, Happer W, Hedlund LW, Johnson GA, Juvan K. MR imaging with hyperpolarized ^3He gas. *Magn Reson Med* 1995;33:271–275.
- Johnson GA, Cates G, Chen XJ, Cofer GP, Driehuys B, Happer W, Hedlund LW, Saam B, Shattuck MD, Swartz J. Dynamics of magnetization in hyperpolarized gas MRI of the lung. *Magn Reson Med* 1997;38:66–71.
- Matter NI, Scott GC, Venook RD, Ungersma SE, Grafendorfer T, Macovski A, Conolly SM. 3D Prepolarized MRI with RARE. In: *Proceedings of the 14th Annual Meeting of ISMRM, Seattle, WA, USA, 2006*.
- Bhagwandien R, Moerland MA, Bakker CJ, Beersma R, Lagendijk JJ. Numerical analysis of the magnetic field for arbitrary magnetic susceptibility distributions in 3D. *Magn Reson Imaging* 1994;12:101–107.
- Li S, Williams GD, Frisk TA, Arnold BW, Smith MB. A computer simulation of the static magnetic field distribution in the human head. *Magn Reson Med* 1995;34:268–275.
- Li L, Leigh JS. Quantifying arbitrary magnetic susceptibility distributions with MR. *Magn Reson Med* 2004;51:1077–1082.
- Haacke EM, Brown RW, Thompson MR, Venkatesan R. *Magnetic resonance imaging: physical principles and sequence design*, 1st ed. New York: Wiley-Liss; 1999.
- Matsuura H, Inoue T, Konno H, Sasaki M, Ogasawara K, Ogawa A. Quantification of susceptibility artifacts produced on high-field magnetic resonance images by various biomaterials used for neurosurgical implants. *J Neurosurg* 2002;97:1472–1475.
- Sofka CM, Potter HG, Figgie M, Laskin R. Magnetic resonance imaging of total knee arthroplasty. *Clin Orthop Relat Res* 2003;129–135.
- Hennig J, Nauwerth A, Friedburg H. RARE imaging: a fast imaging method for clinical MR. *Magn Reson Med* 1986;3:823–833.
- Potter HG, Nestor BJ, Sofka CM, Ho ST, Peters LE, Salvati EA. Magnetic resonance imaging after total hip arthroplasty: evaluation of periprosthetic soft tissue. *J Bone Joint Surg* 2004;86:1947–1954.